ELECTROCHEMISTRY

Solid-state polymer-particle hybrid electrolytes: Structure and electrochemical properties

Nyalaliska W. Utomo[1], Shifeng Hong[2], Ritwick Sinha[1], Keun-il Kim[1], Yue Deng[2], Prince Ochonma[1], Minori G. Kitahata[1], Regina Garcia-Mendez[1], Yong L. Joo[1], Lynden A. Archer[1]*

Solid-state electrolytes (SSEs) are challenged by complex interfacial chemistry and poor ion transport through the interfaces they form with battery electrodes. Here, we investigate a class of SSE composed of micrometer-sized lithium oxide (Li_2O) particles dispersed in a polymerizable 1,3-dioxolane (DOL) liquid. Ring-opening polymerization (ROP) of the DOL by Lewis acid salts inside a battery cell produces polymer-inorganic hybrid electrolytes with gradient properties on both the particle and battery cell length scales. These electrolytes sustain stable charge-discharge behavior in Li||NCM811 and anode-free Cu||NCM811 electrochemical cells. On the particle length scale, Li_2O retards ROP, facilitating efficient ion transport in a fluid-like region near the particle surface. On battery cell length scales, gravity-assisted settling creates physical and electrochemical gradients in the hybrid electrolytes. By means of electrochemical and spectroscopic analyses, we find that Li_2O particles participate in a reversible redox reaction that increases the effective CE in anode-free cells to values approaching 100%, enhancing battery cycle life.

INTRODUCTION

The growing interest in lithium metal as a replacement anode material for the commonly used lithium-infused graphite materials in state-of-the art lithium-ion batteries is reflected by the increasing number of studies and literature reviews (*1*–*5*). It is understood that a key driver of this interest is the nearly 10-fold increase in theoretical specific capacity of the anode achieved by replacing the graphite host with lithium metal (*5*). The combination of the high chemical activity and low reduction potential of Li metal introduces multiple technical barriers that have been thoroughly discussed in several recent reviews (*3*–*5*).

Solid-state electrolytes (SSEs) are generally thought to provide a straightforward strategy toward lithium metal batteries that are safer and less prone to runaway thermal events associated with nonplanar, mossy Li deposition during battery recharge (*6*, *7*). However, these benefits are typically accompanied by sacrificed room temperature ionic conductivity and poor electrode-electrolyte contact. Substantial efforts have been concentrated on overcoming these challenges using solid electrolyte that emerge from wettable precursors (*8*, *9*) and through regulation of ionic pathways throughout SSE's crystal structure design (*9*–*11*). Using Li metal anode also requires a solid electrolyte interphase (SEI) capable of maintaining chemical and mechanical integrity at the high reduction potentials at which Li plates during battery charging, and which protect the freshly deposited Li from continuous loss due to parasitic chemical reactions with electrolyte components (*7*, *12*, *13*).

Inorganic-organic hybrid electrolytes are of particular interest due to their ability to separate the mechanical, ion transport, and interfacial functions of an electrolyte using discrete ingredients with properties optimized for these functions. A consequence is that such electrolytes are unique in their ability to provide combinations of high, liquid-like ionic conductivity and solid-like mechanical strength, comparable to SSEs (*14*). Typically, hybrid electrolytes are created by suspending electrochemically inert particles (typically metal oxides) in an ion-conducting liquid or plasticized polymer host (*15*–*17*). Among the advantages of such materials are their ease of fabrication, straightforward compatibility with normal battery manufacturing methods, and versatility in the chemistry of the suspended particles and suspending electrolyte that can be used. Oxide particles suspended in a liquid electrolyte adsorb ionic species, creating a space charge layer on their surface, which has been thought to facilitate ion-pair dissociation and transport in the electrolyte (*18*). Al_2O_3 particles in solid LiI, for instance, have been reported to adsorb Li^+ on their surface, resulting in an increased vacancy concentration in lithium sublattice that increases the overall conductivity. SiO_2 introduced to PbF_2 has likewise been argued to adsorb F^-, creating fluoride vacancies. These advantages are countered by the generally high interfacial impedances that occur if the particles segregate to the electrode and by the potential for irreversible loss of Li ions that either bind too strongly or which chemically react with the oxide particles.

The majority of studies of suspension electrolytes focus on systems containing electrochemically inert, nanosized particles in the dilute concentration regime (*19*–*22*). Few consider systems composed of larger microspheres capable of spontaneously settling under gravity. Recently Kim *et al.* (*19*) reported that electrolytes created by addition of nanometer-sized Li_2O particles in aprotic liquids containing fluorinated additives sustain reversible cycling of anode-free Cu||NCM811 batteries for at least 30 cycles. By means of cryogenic scanning transmission electron microscopy (cryo-STEM) and electron energy loss spectroscopy (EELS), the authors conclusively showed that the SEI formed at the anode surface is enriched in Li_2O. In addition, by means of density functional calculations, they further showed that the Li_2O particles are surrounded by a solvation layer enriched with F^- ions (*19*).

Recently, we reported that liquid electrolytes based on 1,3-dioxolane (DOL) undergo an $Al(OTf)_3$ Lewis acid–initiated ring-opening polymerization inside a battery cell to create solid polymer electrolytes (SPEs) with room temperature ionic conductivities exceeding 1 mS/cm at $Al(OTf)_3$ concentrations below 1 mM (*8*). Suspension electrolytes created by dispersing poly(ethylene glycol) (PEG)–grafted SiO_2 nanoparticles in DOL were subsequently reported to undergo a similar ring-opening polymerization to create hybrid SPEs (HSPEs) with even

[1]Robert Frederick Smith School of Chemical and Biomolecular Engineering, Cornell University, Ithaca, NY 14853, USA. [2]Department of Materials Science and Engineering, Cornell University, Ithaca, NY 14853, USA.
*Corresponding author. Email: laa25@cornell.edu

higher room temperature ionic conductivity ~4 mS/cm (*9*). It was theorized that interactions between and co-crystallization of the tethered PEO oligomers and poly(DOL) provided more ether oxygen domains to complex with Li^+, which facilitated ion transport. Here, we wish to expand on this concept by creating HSPEs in which electrochemically active particles, such as Li_2O, are used to regulate both the physicochemical properties of the in situ–formed solid-state, poly(DOL) electrolytes in bulk and in the SEI. We show that such electrolytes enable extended cycling of anode-free Cu||NCM811 with low interfacial resistances and effective values of the columbic efficiencies computed by fitting the cycling data to a power law decay function markedly larger than observed in either the unpolymerized or polymerized electrolyte in the absence of the Li_2O particles. The electrolytes also manifest interesting gradient physical and transport properties (i.e., they are solid-like polymers far from the anode surface and are liquid-like near the anode).

RESULTS

A simple force balance (Eq. 1) comparing the gravitational, buoyancy, and thermal force, kT/r, on particles of radius, r, and density, ρ_s, dispersed in a liquid of density ρ_f, indicates that particles with radii above a critical value, $r \geq r_c$ will settle in a suspension to create a two-phase material in which a substantially particle-free liquid phase coexists with a porous, granular material with solvent in its pores. Here, k is Boltzmann constant (1.38×10^{-23} m^2 kg/s^2 K), g the gravitational acceleration (9.8 m/s^2), and T is temperature (303 K). Taking the density of Li_2O as $\rho_s \approx 2$ g/ml at $T = 303$ K, we find that $r_c = 0.62$ μm for the Li_2O/DOL ($\rho_f = 1.32$ g/ml) suspensions and $r_c = 0.57$ μm for the Li_2O/EC ($\rho_f = 1.06$ g/ml) suspensions. Thus, a Li_2O/DOL or Li_2O/EC suspension electrolyte composed of 100-mesh Li_2O microspheres will exist as a two-phase system, a supernatant liquid containing Li_2O particles with sizes less than around 600 nm and a precipitated porous bed formed by gravitational settling of larger particles.

$$r_c = \left[\frac{3kT}{4\pi g(\rho_s - \rho_f)}\right]^{\frac{1}{4}} \quad (1)$$

Results reported in figs. S1 and S3 show that Lewis acid initiated polymerization of Li_2O/DOL suspensions produces a two-phase material in which an Li_2O-lean poly(DOL) layer coexists with a Li_2O-rich liquid DOL layer. We find that if the suspensions are continuously agitated to prevent settling of Li_2O particles, the ring-opening polymerization of DOL is completely arrested. A straightforward explanation of these observations is possible. Lithium oxide (Li_2O) particles are Lewis bases with pH of 10 in Li_2O/DOL suspensions. We note further that Li_2O particles are known to adsorb anionic species on their surfaces (*19*). We conclude that the Li_2O particles neutralize the Lewis acid $Al(OTf)_3$ initiator needed for ring-opening polymerization of DOL. In the absence of mixing, the particle concentration is highest in the gravity preferred direction, which means that DOL polymerization would occur at a progressively lower rate as the concentration of particles rises. In the synthesis cell configuration illustrated in fig. S1A, this would result in an essentially liquid DOL electrolyte near the base of the cell. The liquid DOL electrolyte is in equilibrium with a hybrid Li_2O/poly(DOL) electrolyte with a reduced concentration of Li_2O particles that are too small to settle on the timescale of the polymerization reaction, which is consistent with what is observed.

Analysis of the particle size distribution using an Anton Paar particle size analyzer (PSA) indicates that immediately after mixing the average suspended particle size is 18 ± 0.6 μm (fig. S2). The particles are evidently large enough to spontaneously settle. After a period of approximately 15 min following mixing, gravity-driven settling is observed and a moderately narrower particle size distribution is seen in the supernatant, with particle size plateauing at 25 ± 0.5 μm by the 15th minute. This is also accompanied by a new peak in the distribution associated with much smaller particles with sizes between 1.5 and 2.0 μm. Scanning electron microscopy (SEM) analysis of the settled particle phase reveal that some of the Li_2O particles have sizes as large as 80 μm (fig. S1G). Figure S3 illustrates the gradient property produced by particle settling. The resultant hybrid electrolyte is composed primarily of poly(DOL) with melting points at $T_m = 31$°C and 49°C as well as recrystallization temperature of $T_c = -15$°C. On the other hand, poly(DOL) formed near the settled particles lacks an obvious melting point and its glass transition temperature is shifted to a lower value, which contrasts with previous findings for particle-tethered polymers (*23*, *24*). These observations imply that whereas a lower molecular weight, amorphous polymer is formed by ring-opening polymerization of DOL in the particle-rich sediment, a semicrystalline poly(DOL) material is formed when the polymerization occurs in the Li_2O particle lean supernatant. Thermogravimetric analysis (TGA) suggests that a more liquid-like organic-rich phase results from polymerization of DOL in the particle-rich phase.

To understand how such a two-phase electrolyte might influence reversibility of a Li||NCM811 battery cell or, more challengingly, a Cu||NCM811 anode-free battery cell, we created coin cells with the configurations illustrated in Fig. 1C. The cells were designed with two separators (Celgard 3501, which is manufactured to have micron-sized pores) as illustrated, and the Li/Cu anode oriented in the gravity assisted direction. In assembling the cells, Li_2O/DOL suspension was dropped on the anode side and both separators applied in sequence. A DOL electrolyte containing 1 mM $Al(OTf)_3$ was thereafter applied to the cathode side and the cathode installed to complete the cell assembly.

In situ ring-opening polymerization of Li_2O/DOL electrolytes in such cells would produce materials with distinct characteristics in the separator near the particle-laden anode versus near the particle-lean cathode (Fig. 1C). Analysis by Fourier transform infrared spectroscopy (FTIR) and SEM largely confirm these expectations. FTIR analysis of the separator near the cathode reveals a strong poly(DOL) peak at ~1000 cm^{-1} (*8*, *9*), with no evidence of Li_2O particles (Fig. 1B). The opposite is seen for the separator near the anode, which is rich in Li_2O particles. SEM images reveal notable morphological differences between the two separators. As polymer precursor wets the separator and polymerization happens, the cathode facing separator is seen to lose its porous microstructure as poly(DOL) forms within the pores (Fig. 1E). In contrast the anode-facing separator retains its porous structure (Fig. 1F). Thus, we are able to confirm that the poly(DOL) electrolyte is formed primarily at the battery cathode.

At the highly reducing potentials at which Li^+ is plated at a battery anode, all electrolyte components would be expected to degrade in time. The formation of a well-formed SEI containing inorganic and organic components at the anode is a well-practiced strategy for passivating the electrode to prevent continuous electrolyte degradation (*25*). Li_2O is an SEI component that has been reported in some systems (*26*–*28*). A suspension electrolyte made up of Li_2O suspension is a pathway to create an ideal SEI that protects the anode and, as we will demonstrate, has ionic conduction mechanism closely related to those

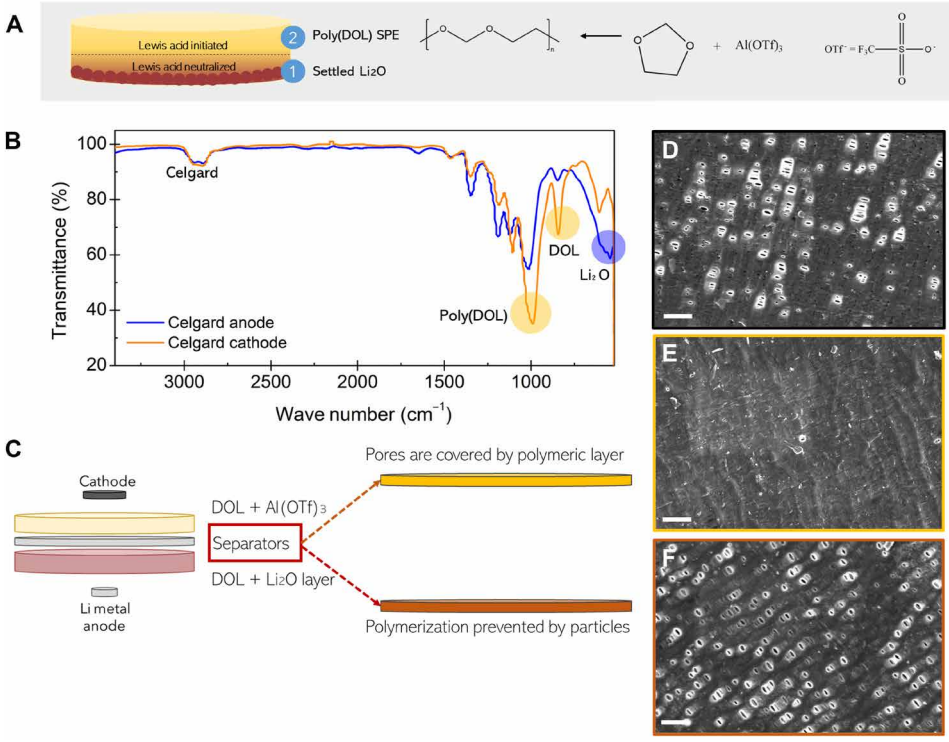

Fig. 1. Gradient property of hybrid electrolyte caused by gravitational settling and basicity of Li_2O microparticles. (**A**) Schematic illustration of method used to synthesize Li_2O/poly(DOL) hybrid electrolytes with attractive gradient properties produced by gravity settling of Li_2O. (**B**) Results from Fourier transform infrared spectroscopy (FTIR) analysis of the anode and cathode facing sections of the separators. (**C**) These separators are taken from the cell design using a pair of Celgard 3501 separators to sequester the particle-rich phase to the region near the Li anode. (**D**) SEM analysis of the structure of the cathode and anode-facing separator surfaces, compared with that of the pristine Celgard material. It is apparent that polymerization of the DOL yields a material that covers the pores on the cathode-facing separator (**E**); however, the separator on the anode side is seen to still retain the porous structure (**F**). All scale bars indicate 2 μm, and larger-scale images are shown in fig. S1.

found in liquid electrolytes. At the other end of the battery, highly oxidized cathode surface tends to create interfacial irreversible reaction between cathode and the electrolyte at high potential. This creates the so-called cathode electrolyte interphase (CEI) that could lead to capacity loss (*29*, *30*). It is then crucial to suppress side reactions of liquid DOL, which has low oxidative stability, to facilitate use in lithium metal batteries (LMBs) based on high-voltage cathodes. This can be done by polymerizing DOL into poly(DOL) near the cathode. The stratification of these two layers, all formed in situ, is an overall pathway in creating more reliable SSEs that fit the anode/cathode duality of batteries.

Oxide particles are conventionally thought to help ion dissociation by adsorbing ionic species and hence create a space charge layer that serves as an ionic conduction pathway (*14*); here, we see no such effects. The strong Lewis basicity of the Li_2O particles might then be expected to exert a large influence on ion transport by facilitating ion pair dissociation. To elucidate the role played by Li_2O on the ion transport properties, we used a simple, theoretical framework attributed to Maxwell (*31*) to describe ionic conductivity data obtained in Li_2O/DOL suspensions electrolytes. The Maxwell analysis has previously been applied to quantitatively explain ion transport in suspension electrolytes under electrochemical driving forces (*32*). The conductivity σ of a suspension of particles with conductivity, σ_p, is related to that of the suspending medium, σ_0, and particle concentration, ϕ, through (Eq. 2). The coefficient α is a function of the suspending medium, σ_0, and particle, σ_p, conductivity (Eq. 3). For perfectly insulating particles, $\sigma_p \ll \sigma_0$, $\alpha = 1/2$ and σ/σ_0 is a function of ϕ only (Eq. 4).

$$\frac{\sigma}{\sigma_0} = \frac{1 - 2\alpha\phi}{1 + \alpha\phi} \tag{2}$$

$$\alpha = \frac{\sigma_0 - \sigma_p}{2\sigma_0 + \sigma_p} \tag{3}$$

$$\frac{\sigma}{\sigma_0} = \frac{2\,(1 - \phi)}{2 + \phi} \tag{4}$$

We measured the temperature-dependent ionic conductivity of Li_2O/DOL electrolytes as a function of ϕ (see fig. S3A) and compare the experimental results with theoretical predictions based on Eq. 4 in Fig. 2A. It is seen that up to a particle concertation of approximately 40 vol %, ion transport in Li_2O/DOL electrolytes are in nearly perfect agreement with the Maxwell model, revealing that the Li_2O particles behave as perfect insulators. We wondered whether these observations are a consequence of the low dielectric constant ($\varepsilon_{DOL} = 19$) of DOL and performed similar experiments using suspension electrolytes in which the same Li_2O particles were dispersed in a solvent, ethylene carbonate (EC), with a substantially higher dielectric constant ($\varepsilon_{EC} = 89.8$). The results reported in fig. S5 again

clearly show agreement with Eq. 4 for particle concentrations up to 40 vol %. In addition, we note that notwithstanding the decrease in ionic conductivity with increasing Li_2O particle volume fraction, no notable changes in the activation energy E_a for ion transport are observed (see fig. S4), especially for suspensions with particle volume fractions 10 vol %. This result confirms that the ion conduction mechanism (*33*–*35*) is essentially unaffected by the Li_2O particles and implies that the ions move primarily via a network formed by the liquid DOL electrolyte.

Like many particulate additives, Li_2O addition offers a degree of mechanical reinforcement. Figure S6 shows results from strain-dependent measurement of Li_2O pure suspensions in liquid DOL containing 1 M LiTFSI, where strain was varied from 0.025 to 10% at a constant angular frequency. Storage G' and loss G'' moduli reflect the solid-like and viscous-like contributions within the material, and both increase with increasing Li_2O particle concentration. G' shows value as high as 100 Pa for 10 vol %, comparable to those of low–molecular weight polymers or oligomers used as polymer electrolytes (*36*). Increasing Li_2O concentration to 30 vol % causes G' to have a value of 1000 Pa. As suspension reaches 50 vol %, G' of 4×10^5 Pa is observed. This very high modulus is comparable to values typically observed in crystalline polymers or soft materials close to their glass/jamming transition (*37*).

The increase in mechanical strength is also accompanied by changes in the stress-strain curve. Materials that manifest a yield point typically first display a linear stress-strain response before yielding alters the slope of the stress-strain curve (*38*). Many suspensions are known to have yield stress, and the denser the suspensions, the more likely yielding occurs as it takes a certain degree of deformation for particles to move and get out of their "cages." Suspension with 10 vol % Li_2O does not exhibit any yield stress, but increasing particle concentration causes yielding behavior in the suspension. The yield stress value τ_y, taken from the point where deviation from linearity in the stress-strain curve happens, increases with increasing particle concentration and eventually reaching $\tau_y \approx 100$ Pa at 50 vol % Li_2O content. The more tortuous pathway due to particle aggregation likely causes deviation from Maxwell prediction and explains the declining conductivity value with increasing volume fraction (Fig. 2A).

Hybrid electrolytes created by polymerizing DOL containing Li_2O particles using the method shown in Fig. 1A manifest higher ionic conductivity values than both precursor materials (Fig. 2, B and C). The hybrid electrolyte for example exhibits an ionic conductivity value of $\sigma = 4.3$ mS/cm at 30°C, while pure poly(DOL) and pure suspension have $\sigma = 2.4$ and 3.2 mS/cm, respectively. The enhanced conductivity values (>1 mS/cm) remain even at temperatures as low as −30°C. It is interesting that such high low-temperature ionic conductivity values are unattainable for the semicrystalline poly(DOL) electrolyte. Furthermore, the hybrid electrolytes manifest the lowest activation energy E_a of 4.2 ± 0.2 kJ/mol compared to pure poly(DOL) (E_a = 6.9 ± 0.2 kJ/mol) and pure suspension (E_a = 4.6 ± 0.3 kJ/mol). E_a values are calculated through Arrhenius equation $\sigma = Ae^{-Ea/RT}$ with A being a pre-exponential factor, R universal gas constant, and T temperature.

The hybrid electrolyte conductivity is seen to evolve with polymerization time, with conductivity value first increasing and ultimately plateauing after around 5 hours of polymerization. Temperature-dependent conductivity at the 1st, 5th, 10th, 24th, and 96th hour is shown in Fig. 2D. A key finding is that the discontinuous transition in conductivity seen in the first hour, gaping below and above 30°C, indicated by two

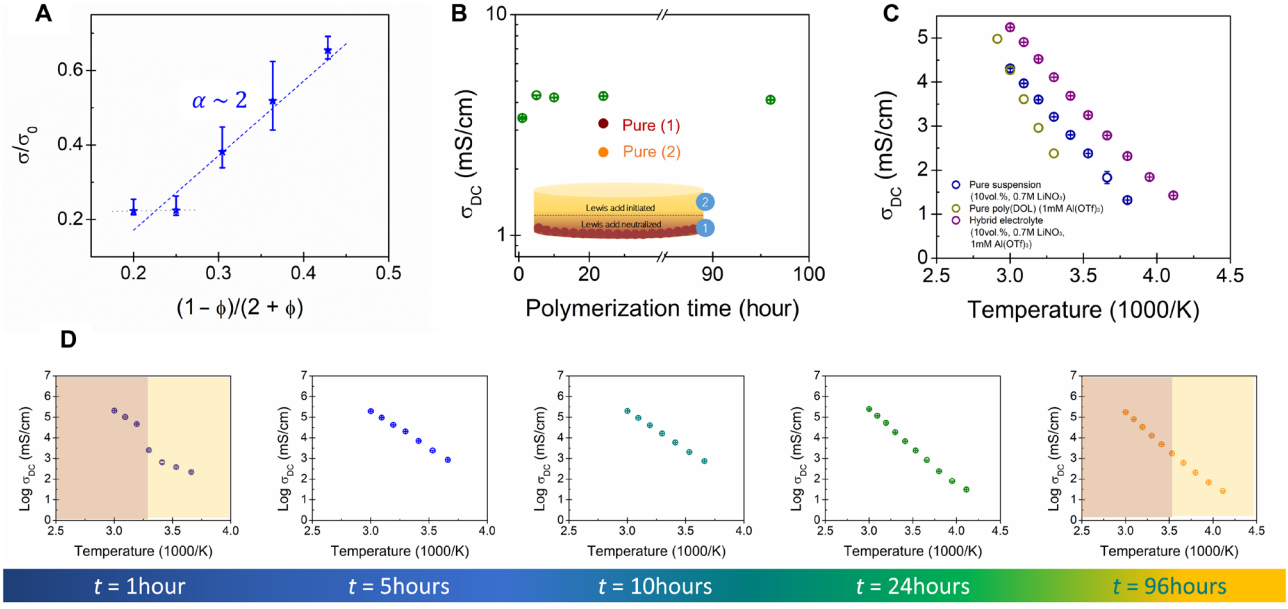

Fig. 2. Ionic conduction mechanism and ionic conductivity values of hybrid Li_2O/DOL and Li_2O/poly(DOL) electrolytes with temperature and time. (**A**) Normalized ionic conductivity value following Maxwell model for Li_2O/DOL suspension electrolytes at various volume fractions. Data points seen are averaged from the conductivity values obtained at different temperatures, as shown in fig. S4. (**B**) As polymerization of a Li_2O/DOL hybrid electrolyte [first layer, 10N7; second layer, poly(DOL) + 2 M LiTFSI + 1 mM $Al(OTf)_3$], proceeds with time, the ionic conductivity measured at 30°C first rises and stabilizes at values higher than observed either for the precursor Li_2O/DOL suspension or pure poly(DOL) electrolyte with the same salt concentration. (**C**) Temperature-dependent ionic conductivity values for in situ–formed Li_2O/poly(DOL) hybrid electrolyte, for a Li_2O/DOL suspension electrolyte, and for in situ–formed poly(DOL) electrolyte. (**D**) Temperature-dependent changes in ionic conductivity of an in situ–formed Li_2O/poly(DOL) hybrid electrolyte as a function of time following the onset of polymerization.

shaded regimes in the figure largely eases as polymerization progresses with time, as seen in the continuous trend at 96th hour. We have previously reported a shift from a Vogel-Fulcher-Tamman–like behavior of amorphous poly(DOL) hybrid electrolyte to an Arrhenius one as crystallization of poly(DOL) takes place (*9*). As crystallization and associated chain reconfiguration in semicrystalline polymers typically produce large changes in the conduction mechanism near the melting point or glass transition temperature T_g (*34*). Discontinuous changes in ionic conductivity have been reported extensively to accompany thermal transitions in a range of electrolytes (*42*–*45*). Stratification of polydisperse microsphere suspension has been extensively examined (*42*, *43*); larger particles settle, and smaller ones get suspended in liquids. This is also what we observed through TGA (see fig. S3B), with a concentration gradient increasing toward the plane of highest gravitational force. The stratification process is a time-dependent process, with the system shifting from a nonequilibrium state to an equilibrium, stratified one (*42*).

To evaluate the electrochemical features of the hybrid electrolytes, we studied Li_2O/DOL suspension electrolytes containing 10 vol % (Fig. 3A) and 50 vol % Li_2O (Fig. 3B) and 2 M LiTFSI in Li||NCM811 full and Li||Cu half cells. A fixed current density of 1 mA/cm^2 was used for these experiments. The results reveal that at either of the Li_2O concentrations studied, the cells cycle stably, reaching a discharge capacity of 1.45 mAh/cm^2 by 100 cycles (Fig. 3C). Before cycling, cells were subjected to a SEI buildup process at a low current density of C/10 for the first five cycles. The results are also interesting because DOL is not commonly used as a stand-alone electrolyte solvent in LMBs due to their poor oxidative stability (<4 V) and chemical instability with the most used lithium salts, like $LiPF_6$ (*44*).

Results in Fig. 3 (D and E) reveal that notwithstanding the uniform stable cycling observed, the coulombic efficiency (CE) and morphology of plated lithium metal varies with Li_2O volume fraction (fig. S7). SEM analysis of the Cu electrode harvested from the Li||Cu half cells after depositing 10 mAh/cm^2 Li on the copper reveal that the relationship between electrodeposit morphology and Li_2O concentration is nonmonotonic. Specifically, the roughest Li deposits are observed for the pure DOL electrolyte, followed by electrolytes containing 50, 30, and 10 vol % Li_2O. The trend is not the same for the CE measured in Li||Cu cells. These measurements show that the CE rises from 98.0% for cells containing the pure DOL electrolyte to 98.8% for cells containing suspension electrolytes with 10 vol % Li_2O (Fig. 3D). CE further increases to 99.2% for electrolytes containing 20 vol % Li_2O and changes negligibly thereafter with increasing Li_2O concentration. Nyquist plots reported in (fig. S8) indicate that both the coarser lithium deposits and plateauing CE values coincide with an increase in interfacial resistance at higher Li_2O particle concentrations.

Anode-free lithium cells provide a particularly challenging testbed for evaluating the attributes of any hybrid or SSE. Because Li metal is not present during cell assembly, an anode-free LMB is also viewed as attractive from a practical point of view because it removes safety issues involved in handling lithium metal in a manufacturing setting (*45*–*47*) and enhances the battery's energy density as the electrode weight is reduced. Reliable anode-free LMBs are presently hindered by the low CE due to interfacial reactivity, transport associated with the nonuniform deposition of lithium as well as its parasitic chemical and electrochemical reactions with electrolyte components (*45*). Figure 4A reports the galvanostatic cycling of Cu||NCM811 cells

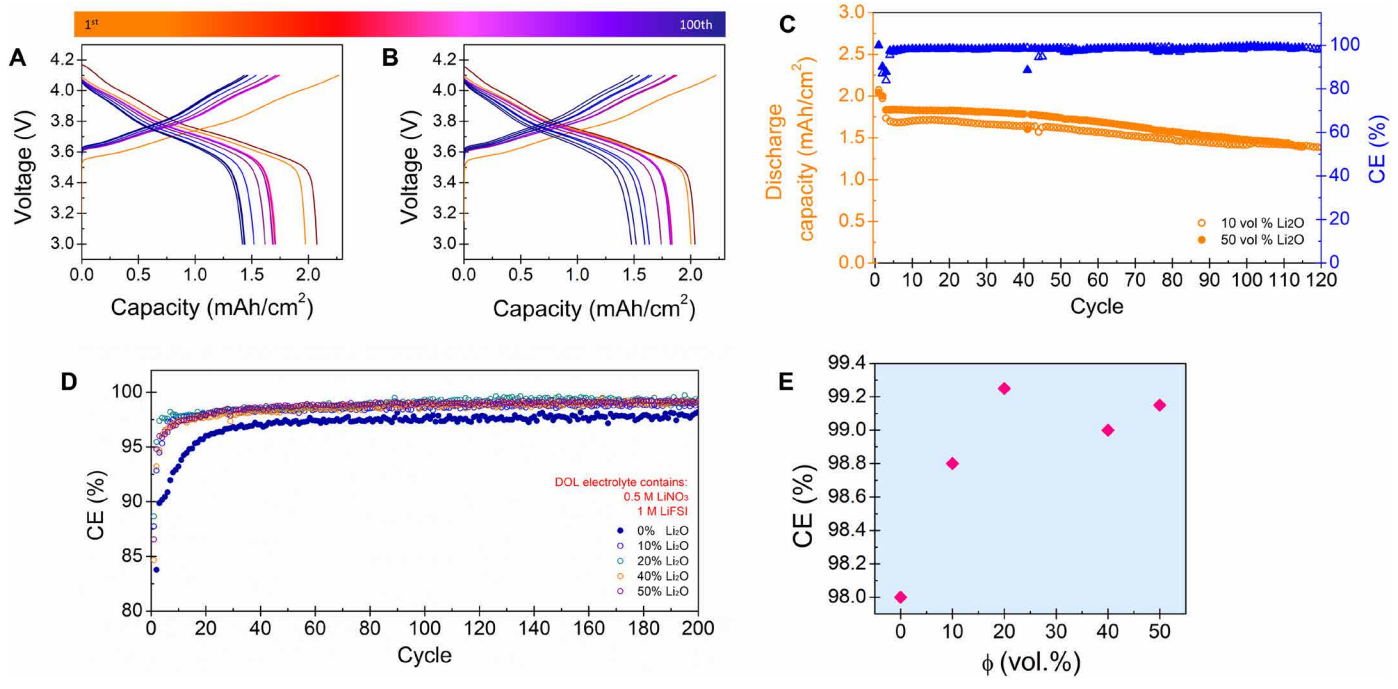

Fig. 3. Electrochemical performance of Li_2O/DOL suspension electrolyte. (**A**) Galvanostatic charge and discharge of Li||NCM811 in hybrid Li_2O/DOL electrolytes containing 10 vol % and (**B**) 50 vol % Li_2O and 2 M LiTFSI. (**C**) The discharge capacity and coulombic efficiency (CE) of the cells in (A) and (B) over 120 cycles. Cells were run with Li||NCM811 configuration at C/10 for the first five cycles, followed by 1C for the rest of the cycle. (**D**) CE obtained in Li||Cu half-cells configuration for different Li_2O volumetric concentrations. The resulting CE value at each concentration is presented in (**E**).

containing hybrid electrolytes created by ring-opening polymerization of a 10% Li_2O/DOL suspension containing 1 mM $Al(OTf)_3$ + 2 M LiTFSI + 0.5 M $LiNO_3$. This electrolyte is identified as 10N5 in what follows exhibits a nearly constant CE value of 97% and a first-cycle discharge capacity of approximately 1.4 mAh/cm^2 at a cycling rate of C/2. As illustrated in Fig. 4B, the discharge capacity of the cells decreases gradually with cycling, but the rate of decrease is substantially lower than observed in previous studies of anode-free LMBs and markedly lower than for anode-free cells based on the control electrolytes (i.e., DOL and Li_2O/DOL suspension electrolytes) (see also fig. S9), underscoring the benefits of polymerization of the DOL. As illustrated in Fig. 4C, the results reported in Fig. 4B are remarkable for another reason. Specifically, for an anode-free battery cell that runs with a nearly constant CE, the discharge capacity at the nth cycle is related to the value at the first cycle ($n = 1$), as a simple power law of CE

$$\mathrm{CE}^n = \frac{\mathrm{Capacity}_n}{\mathrm{Capacity}_{n=1}} \tag{5}$$

The dashed line in Fig. 4C was obtained using Eq. 5, with the value estimated from the experimentally measured discharge and charge capacity per cycle (CE ≈ 0.97) inserted in the expression. A plot of $\log\left(\frac{\mathrm{Capacity}_n}{\mathrm{Capacity}_{n=1}}\right)$ against n linearizes Eq. 5, with the slope equal to log CE. Comparing this line to the actual discharge capacity measured for the anode-free cells, a large discrepancy is observed. Namely, the anode-free cells containing the hybrid electrolyte show more efficient utilization of the Li stored in the cathode. We fitted the experimentally determined capacities to the linearized version of Eq. 5 and extracted the CE value required to obtain the best fit. It is apparent that the effective CE ≈ 0.994 of the cells is much closer to unity. We estimated the apparent increment in CE at each cycle by taking

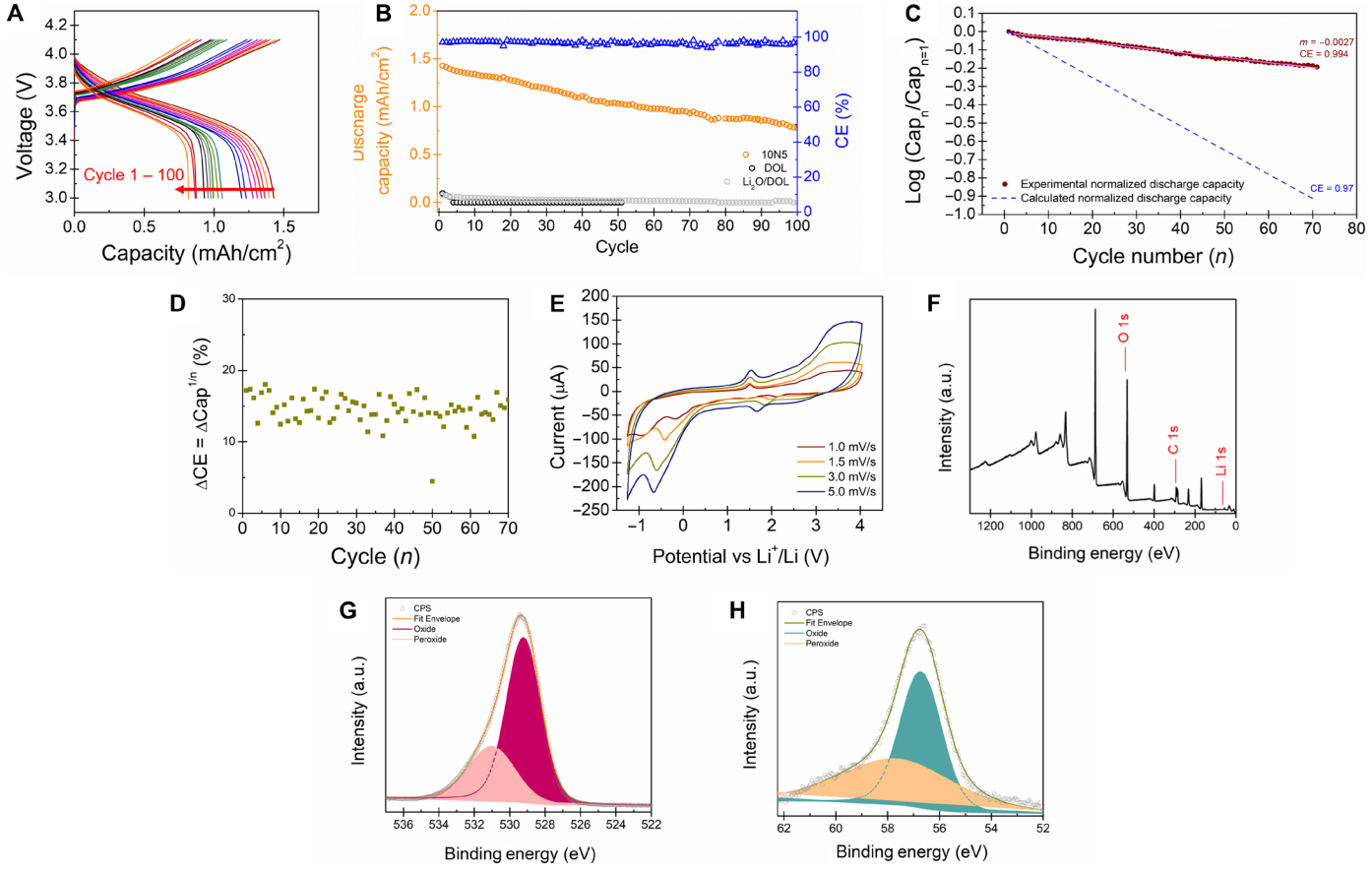

Fig. 4. Effects of the electroactive Li_2O toward the application of anode-free Li-battery. (**A**) Galvanostatic cycling performance and electrochemical properties of anode-free Cu||NCM811 cells based on Li_2O/poly(DOL) electrolytes for 10 vol % Li_2O. The poly(DOL) was polymerized inside the battery cell using 1 mM $Al(OTf)_3$ and the cells were cycled at a rate of 0.5 mA/cm^2 (C/2). For the results in (A), a salt blend consisting of 2 M LiTFSI + 0.5 M $LiNO_3$ (here termed N5) was used. The respective discharge capacities and CE values are reported in (B). Included in (**B**) are discharge capacity values of DOL + 2 M LiTFSI electrolyte without and with the addition of 10 vol % Li_2O, cycled at C/10 for 5 cycles and a comparable C/2 rate for the rest of the cycles. SEI buildup during the formation step at C/10 is detailed in fig. S12. CE values are used to predict capacity fading shown in the dashed line of (**C**), while solid data points show actual capacity fading. The difference between CE of this electrolyte and a control DOL + 2 M LiTFSI electrolyte is shown in (**D**). The corresponding Li||NCM811 cell performance for the same electrolyte as in (A) is shown in fig. S11. (**E**) Cyclic voltammetry (CV) measured in cells in which Li_2O particles in a carbon cloth (CC) current collector are paired with Cu-foil in a DOL + 2 M LiTFSI electrolyte. (**F**) X-ray photoelectron spectroscopy (XPS) of Li_2O@CC electrode post-CV and held at oxidation potential for 5 hours, indicating existence of oxygen, carbon, and lithium. a.u., arbitrary units. Two peaks attributed to lithium oxide (Li_2O) and lithium peroxide (Li_2O_2) are seen in the (**G**) O scan and (**H**) Li scan.

the *n*th root difference of the discharge capacity measured in the anode-free cells cycled in the control electrolyte from those measured in the10N5 hybrid electrolyte. This analysis reveals a relatively stable increment of around 15% at each cycle (fig. 4D).

We hypothesized that in addition to the role in reinforcing mechanical properties of the hybrid electrolytes, in retarding polymerization of DOL, and in producing gradient properties in the hybrid electrolytes, the Li_2O particles contribute some amount of Li to compensate for losses each cycle. As partial confirmation of the hypothesis, fig. S10 reports results from galvanostatic cycling of a Li||NCM811 cell that uses the 10N5 electrolyte under the same conditions used for the measurements reported in Fig. 4A. The presence of excess Li in the cells clearly improves their cycling. As a more direct test of the hypothesis, we performed x-ray diffraction (XRD) and Raman spectroscopic analysis of Cu anodes harvested from the cycled cells. The results reported in fig. S12 support formation of Li_2O_2 in the electrodes, but the signals are relatively weak. To assess the role of the Li_2O in this process and to evaluate the reversibility of the formed Li_2O_2 under our cell running conditions, we performed extensive cyclic voltammetry measurements using Li_2O||Cu cells (see Fig. 4E). The Li_2O electrodes used for these studies were created by sandwiching Li_2O particles between carbon cloth (CC) as a current collector and using liquid DOL + 2 M LiTFSI as the electrolyte. Three peaks are evident in the cyclic voltammograms, with peak (3) attributed to decomposition of the liquid electrolyte. CV results for control CC||Cu cells using the same electrolyte show an irreversible reduction peak at ~ −3.0 V, and no observable peaks (1) and (2) (fig. S11A). These peaks are then attributed to the oxidation (1) and reduction (2) of Li_2O. The voltammograms also indicate that the peaks currents increase approximately as the square root of scan rate (fig. S11A), indicating that the reactions are transport limited. Our findings are consistent with previous reports which show that Li_2O undergoes an oxidation reaction during discharging to form Li_2O_2, a prominent reaction in Lithium-air battery systems (*48*, *49*).

Additional support comes from x-ray photoelectron spectroscopy (XPS) analysis of the Li_2O electrodes used for the CV experiments. Results reported in Fig. 4 (F to H) were obtained by holding the Li_2O electrodes at an oxidizing potential of approximately 1.5 V (versus Li^+/Li) for 5 hours. The high-resolution O 1s spectra were deconvoluted into two primary peaks centered at 531 ± 0.4 eV and 529 ± 0.3 eV, which indicate oxide (Li_2O) and peroxide (Li_2O_2) bonding modalities respectively (*50*, *51*). An average of three measurements (table S1) revealed a 2:3 ratio of peroxide to oxide on the surface (up to 10 nm scanning depth). These observations were further corroborated by high-resolution Li 1s scans, deconvoluted into two peaks centered at 53.3 ± 0.2 eV for Li_2O and 54.4 ± 0.4 eV for Li_2O_2, which also indicate a 2:3 distribution.

$$E = E^0 + \frac{RT}{nF}\ln\frac{[Ox]}{[Red]} \quad (6)$$

$$|E_p - E_{p/2}| = 2.2\frac{RT}{nF} = \frac{57}{n}\ \text{mV} \quad (7)$$

The $2Li_2O \rightarrow Li_2O_2 + 2Li^+ + 2e^-$ reaction is also seen to be reversible in the DOL electrolyte. The Nernst equation (Eq. 6) can also be used to see the reversibility of the redox reaction. It relates the potential of an electrochemical cell E to the standard potential of a species E^0, as well as the relative activities of oxidized/reduced analyte at equilibrium. R is universal gas constant, F is Faraday's constant, n is the number of electrons, and T is temperature. Estimating E^0 as half-peak potential $E_{p/2}$ and taking E as the potential at the peak current E_p, it is straightforward to conclude that reversible redox reactions should have a value of 57 mV at $T = 25°C$ (Eq. 7) (*52*). The results in fig. S11C reveal that for peaks (1) and (2), these values are 39 and 43 mV, respectively. The charge provided by the redox reaction, quantified by the area under the *i*-*V* curve, is shown to be approximately equal (fig. S11C) indicative of a reversible reaction.

To evaluate the longer-term, electrochemical fitness of the anode free cells, we subjected cells cycled at a fixed rate of C/2 for 100 cycles, to varying rates: 1C and 2C before returning it to the original current rate to C/2. The results reported in fig. S13 show that the cells remain stable and that more than 92% of the capacity measured at the 100th cycle is recovered at the 140th cycle, when the C/2 rate is restored. We also investigated the combined effects of Li_2O particle concentration and $LiNO_3$ concentration on galvanostatic cycling of the anode-free Cu||NCM811 cells. The results reported in fig. S14 show that a higher concentration of Li_2O or $LiNO_3$ increases the CE, but lowers the discharge capacity, which is accompanied by a higher overpotential. Other effects of $LiNO_3$ has previously been explored (*42*, *50*) and is further explored for our system in fig. S16. Consistent with the results reported in Fig. 4 for hybrid electrolytes with 10% Li_2O, results reported in fig. S15 show that a best fit line to the linearized form of Eq. 4 again shows effective CE is increased when Li_2O particles are present in the electrolyte.

DISCUSSION

Suspension electrolytes made up of micrometer-sized Li_2O particles in DOL undergo $Al(OTf)_3$ Lewis acid–initiated ring-opening polymerization inside a battery cell to create hybrid SSEs with room temperature ionic conductivities exceeding 1 mS/cm and beneficial gradient properties. The gradient properties are thought to arise from neutralization of the Lewis acid initiator by the basic Li_2O particles. Gravitational settling of the Li_2O particles is shown to drive macrophase separation, which in turn results in gradients in polymerization inside the cell. Likewise, retardation of ring-opening near the surface of Li_2O particles creates a region of limited or no polymerization near the Li_2O particle surfaces, yielding solid-state materials with room temperature ionic conductivity exceeding 4 mS/cm. This behavior contrasts markedly with observations in Li_2O/DOL suspension electrolytes, which manifest simple Maxwellian conductivity in which particles act as simple insulating inclusions in the liquid DOL host. Used as electrolytes in conventional Li||NCM81, as well as anode-free Cu||NCM811 cells, the hybrid electrolytes enable extended long-term cycling. Curiously, we find that the cycling achieved in the anode-free cells is substantially better than expected from the nominal CEs deduced from their charge/discharge characteristic. We fit the cycling profiles to a power law and estimate the effective CE in the cells to be 99% or higher, indicating that cycling benefits from a source of Li other than the NCM811 cathode. By means of cyclic voltammetry and spectroscopic analysis, we show that reversible redox reaction of the Li_2O particles localized near the anode contribute a small amount of Li each cycle that compensates to an extent for the normal parasitic losses, extending the cycle life of the anode free cells to levels heretofore unseen in the literature.

MATERIALS AND METHODS

Electrolyte and battery preparation

To fundamentally understand the source of the enhanced CE extended cycling of anode-free lithium battery cells, we investigated thermal, transport, and electrochemical properties of Li_2O/poly(DOL) and Li_2O/DOL electrolytes, as well as their analogous Li_2O-free electrolyte controls. Acknowledging the importance of CEI for high-voltage batteries (*29*, *30*) and anodic SEI for batteries with better cycling stability (*7*, *12*, *13*, *25*), hybrid SSEs formed by ring-opening polymerization of Li_2O/DOL suspension electrolyte using a Lewis acid initiator is of particular interest. To fabricate such electrolytes in Li||NCM811 and so-called anode free, Cu||NCM811, cells we first created Li_2O/DOL suspensions (see Fig. 1A). The Li_2O particles (100 mesh, $r_{avg} \leq 150$ μm) was purchased from BeanTown Chemical and used as obtained. Electrolytes suitable for electrochemical studies were created by adding a combination of two salts (LiTFSI and $LiNO_3$) known from previous studies (*40*) to work in tandem to enable formation of good interphases on Li; the studies reported herein used electrolytes comprised either of 2 M LiTFSI + 0.5 M $LiNO_3$ (N5) or 2 M LiTFSI + 0.7 M $LiNO_3$ (N7). Different volume fractions of added Li_2O were used, and the hybrid electrolytes with *x* vol % are denoted as either *x*N5 or *x*N7 (10 vol % in N7 electrolyte is denoted as 10N7). A similar strategy was used to create Li_2O/EC electrolytes for comparison studies. DOL, EC, and LiTFSI were purchased from Sigma-Aldrich and $LiNO_3$ was purchased from Chem-Impex International. Suspension electrolytes with Li_2O particles in either N5 or N7 were first dropped onto Cu foil and a Celgard 3501 separator was placed on top of the suspension. Another Celgard 3501 separator was used and DOL with 2 M LiTFSI was added. To create solid-state Li_2O/poly(DOL) hybrid electrolytes, we introduced 1 mM of the Lewis acid initiator, $Al(OTf)_3$ to the top layer of DOL electrolyte. Poly(DOL) used throughout this study was polymerized by 2 M LiTFSI and 1 mM $Al(OTf)_3$. By varying the concentration of Li_2O from 10 to 50 vol %, hybrid poly(DOL) electrolytes with a range of physical and electrochemical properties were facilely created. The hybrid electrolyte on Cu foil was paired with nickel cobalt manganese oxide (NCM811) cathode obtained from NEI Corporation, and coin 2302-type cells were assembled. All cells were rested for 10 hours before any electrochemical testing as polymerization concludes over time, outlined by previous kinetics studies (*9*).

Material characterizations

FTIR spectra were characterized using a Thermo Fisher Scientific spectrometer in the attenuated total reflection mode. The porous morphology of Celgard separators was imaged by field emission Zeiss Gemini 500 SEM. DC conductivity measurement was carried out using Novocontrol broadband dielectric/impedance spectrometer in the same coin 2032 cells without electrodes and Teflon ring instead of separators. Oscillatory shear measurements were performed using strain-controlled ARES-LS rheometer (Rheometric Scientific) with a cone and plate geometry (10 mm, 4° cone angle and 25 mm, and 1° cone angle). TGA was conducted using TA Instruments Q500 under nitrogen atmosphere at 10°C/min ramping rate. TA Instruments Differential Scanning Calorimetry Auto 2500 was used to evaluate thermal transitions under nitrogen flow at 10°C/min ramping rate. XRD tests were conducted on a Bruker D8 Discover powder diffractometer using Cu Kα radiation of approximate wavelength $\lambda = 1.54$ Å. XPS was performed using Thermo Fisher Scientific Nexsa G2 X-Ray Photoelectron Spectrometer, with operating pressure of approximately 10^{-10} torr, monochromatic Al Kα x-rays at 1486.6 eV, with 400 μm diameter analysis spot. A flood gun was used for charge neutralization of nonconductive samples; all samples were charge corrected using adventitious carbon binding energy (284.8 eV). Raman spectra were collected using a WITec-Alpha 300R confocal Raman microscope. A 532-nm green laser was used, a grating of 1200 liter/mm (± 1 cm^{-1}), 15 accumulations, and 30-s integration time. Particle size analysis was done by Anton Paar PSA (1190) using laser diffraction in liquid dispersion of Li_2O/DOL with concentration of ~5 vol %. Stirring and sonication were done within the first minute of measurement and stopped to measure particle size over time every minute for 15 min.

Electrochemical testing

Galvanostatic stripping/plating tests were performed using Neware CT-3008 battery tester at room temperature. Electrochemical impedance spectroscopy measurements were performed by Solartron Frequency Response Analyzer (Model 1252) with frequencies ranging from 50 kHz to 10 MHz and at an amplitude of 10 mV. Cyclic voltammetry was performed on BioLogic SP-200 potentiostat.

Supplementary Materials

This PDF file includes:

Figs. S1 to S16
Table S1

REFERENCES AND NOTES

1. B. Liu, J.-G. Zhang, W. Xu, Advancing lithium metal batteries. *Joule* **2**, 833–845 (2018).
2. X.-B. Cheng, R. Zhang, C.-Z. Zhao, Q. Zhang, Toward safe lithium metal anode in rechargeable batteries: A review. *Chem. Rev.* **117**, 10403–10473 (2017).
3. J. Liu, Z. Bao, Y. Cui, E. J. Dufek, J. B. Goodenough, P. Khalifah, Q. Li, B. Y. Liaw, P. Liu, A. Manthiram, Y. S. Meng, V. R. Subramanian, M. F. Toney, V. V. Viswanathan, M. S. Whittingham, J. Xiao, W. Xu, J. Yang, X. Q. Yang, J. G. Zhang, Pathways for practical high-energy long-cycling lithium metal batteries. *Nat. Energy* **4**, 180–186 (2019).
4. J. Zheng, M. S. Kim, Z. Tu, S. Choudhury, T. Tang, L. A. Archer, Regulating electrodeposition morphology of lithium: Towards commercially relevant secondary Li metal batteries. *Chem. Soc. Rev.* **49**, 2701–2750 (2020).
5. D. Lin, Y. Liu, Y. Cui, Reviving the lithium metal anode for high-energy batteries. *Nat. Nanotechnol.* **12**, 194–206 (2017).
6. A. Manthiram, X. Yu, S. Wang, Lithium battery chemistries enabled by solid-state electrolytes. *Nat. Rev. Mater.* **2**, 16103 (2017).
7. Q. Zhao, S. Stalin, C.-Z. Zhao, L. A. Archer, Designing solid-state electrolytes for safe, energy-dense batteries. *Nat. Rev. Mater.* **5**, 229–252 (2020).
8. Q. Zhao, X. Liu, S. Stalin, K. Khan, L. A. Archer, Solid-state polymer electrolytes with in-built fast interfacial transport for secondary lithium batteries. *Nat. Energy* **4**, 365–373 (2019).
9. N. W. Utomo, Y. Deng, Q. Zhao, X. Liu, L. A. Archer, Structure and evolution of quasi-solid-state hybrid electrolytes formed inside electrochemical cells. *Adv. Mater.* **34**, e2110333 (2022).
10. Y. Yan, R. S. Kühnel, A. Remhof, L. Duchêne, E. C. Reyes, D. Rentsch, Z. Łodziana, C. Battaglia, A lithium amide-borohydride solid-state electrolyte with lithium-ion conductivities comparable to liquid electrolytes. *Adv. Energy Mater.* **7**, 1700294 (2017).
11. C. Yu, Y. Li, M. Willans, Y. Zhao, K. R. Adair, F. Zhao, W. Li, S. Deng, J. Liang, M. N. Banis, R. Li, H. Huang, L. Zhang, R. Yang, S. Lu, Y. Huang, X. Sun, Superionic conductivity in lithium argyrodite solid-state electrolyte by controlled Cl-doping. *Nano Energy* **69**, 104396 (2020).
12. L. Suo, D. Oh, Y. Lin, Z. Zhuo, O. Borodin, T. Gao, F. Wang, A. Kushima, Z. Wang, H. C. Kim, Y. Qi, W. Yang, F. Pan, J. Li, K. Xu, C. Wang, How solid-electrolyte interphase forms in aqueous electrolytes. *J. Am. Chem. Soc.* **139**, 18670–18680 (2017).
13. P. Verma, P. Maire, P. Novák, A review of the features and analyses of the solid electrolyte interphase in Li-ion batteries. *Electrochim. Acta* **55**, 6332–6341 (2010).
14. A. J. Bhattacharyya, M. Patel, S. K. das, Soft matter lithium salt electrolytes: Ion conduction and application to rechargeable batteries. *Monatsh. Chem.* **140**, 1001–1010 (2009).
15. G. B. Appetecchi, Y. Aihara, B. Scrosati, Investigation of swelling phenomena in PEO-based polymer electrolytes. II. Chemical and electrochemical characterization. *Solid State Ion.* **170**, 63–72 (2004).
16. L.-Z. Fan, Y.-S. Hu, A. J. Bhattacharyya, J. Maier, J., Succinonitrile as a versatile additive for polymer electrolytes. *Adv. Funct. Mater.* **17**, 2800–2807 (2007).

17. S. Choudhury, A. Agrawal, S. Wei, E. Jeng, L. A. Archer, Hybrid hairy nanoparticle electrolytes stabilizing lithium metal batteries. *Chem. Mater.* **28**, 2147–2157 (2016).
18. J. Maier, Ionic conduction in space charge regions. *Prog. Solid State Chem.* **23**, 171–263 (1995).
19. M. S. Kim, Z. Zhang, P. E. Rudnicki, Z. Yu, J. Wang, H. Wang, S. T. Oyakhire, Y. Chen, S. C. Kim, W. Zhang, D. T. Boyle, X. Kong, R. Xu, Z. Huang, W. Huang, S. F. Bent, L. W. Wang, J. Qin, Z. Bao, Y. Cui, Suspension electrolyte with modified Li+ solvation environment for lithium metal batteries. *Nat. Mater.* **21**, 445–454 (2022).
20. S. K. Das, S. S. Mandal, A. J. Bhattacharyya, Ionic conductivity, mechanical strength and Li-ion battery performance of mono-functional and bi-functional ('Janus') 'Soggy Sand' electrolytes. *Energ. Environ. Sci.* **4**, 1391 (2011).
21. A. J. Bhattacharyya, J. Maier, R. Bock, F. F. Lange, New class of soft matter electrolytes obtained via heterogeneous doping: Percolation effects in 'Soggy Sand' electrolytes. *Solid State Ion.* **177**, 2565–2568 (2006).
22. M. S. Kim, Z. Zhang, J. Wang, S. T. Oyakhire, S. C. Kim, Z. Yu, Y. Chen, D. T. Boyle, Y. Ye, Z. Huang, W. Zhang, R. Xu, P. Sayavong, S. F. Bent, J. Qin, Z. Bao, Y. Cui, Revealing the multifunctions of Li_3N in the suspension electrolyte for lithium metal batteries. *ACS Nano* **17**, 3168–3180 (2023).
23. D. Kim, S. Srivastava, S. Narayanan, L. A. Archer, Polymer nanocomposites: Polymer and particle dynamics. *Soft Matter* **8**, 10813–10818 (2012).
24. S. Kim, R. Mangal, L. A. Archer, Relaxation dynamics of nanoparticle-tethered polymer chains. *Macromolecules* **48**, 6280–6293 (2015).
25. E. Peled, The electrochemical behavior of alkali and alkaline earth metals in nonaqueous battery systems—The solid electrolyte interphase model. *J. Electrochem. Soc.* **126**, 2047–2051 (1979).
26. E. Peled, D. Bar Tow, A. Merson, A. Gladkich, L. Burstein, D. Golodnitsky, Composition, depth profiles and lateral distribution of materials in the SEI built on HOPG-TOF SIMS and XPS studies. *J. Power Sources* **97–98**, 52–57 (2001).
27. K. Morigaki, A. Ohta, A., Analysis of the surface of lithium in organic electrolyte by atomic force microscopy, fourier transform infrared spectroscopy and scanning auger electron microscopy. *J. Power Sources* **76**, 159–166 (1998).
28. K. Edström, M. Herstedt, D. P. Abraham, A new look at the solid electrolyte interphase on graphite anodes in Li-ion batteries. *J. Power Sources* **153**, 380–384 (2006).
29. S. J. An, J. Li, C. Daniel, D. Mohanty, S. Nagpure, D. L. Wood III, The state of understanding of the lithium-ion-battery graphite solid electrolyte interphase (SEI) and its relationship to formation cycling. *Carbon* **105**, 52–76 (2016).
30. J.-N. Zhang, Q. Li, Y. Wang, J. Zheng, X. Yu, H. Li, Dynamic evolution of cathode electrolyte interphase (CEI) on high voltage $LiCoO_2$ cathode and its interaction with Li anode. *Energy Storage Mater.* **14**, 1–7 (2018).
31. J. C. Maxwell, *Treatise On Electricity And Magnetism*, (Oxford, Clarendon Press, 1873).
32. J. L. Schaefer, S. S. Moganty, D. A. Yanga, L. A. Archer, Nanoporous hybrid electrolytes. *J. Mater. Chem.* **21**, 10094–10094 (2011).
33. J. C. Bachman, S. Muy, A. Grimaud, H. H. Chang, N. Pour, S. F. Lux, O. Paschos, F. Maglia, S. Lupart, P. Lamp, L. Giordano, Y. Shao-Horn, Inorganic solid-state electrolytes for lithium batteries: Mechanisms and properties governing ion conduction. *Chem. Rev.* **116**, 140–162 (2016).
34. J. Przyluski, M. Siekierski, W. Wieczorek, Effective medium theory in studies of conductivity of composite polymeric electrolytes. *Electrochim. Acta* **40**, 2101–2108 (1995).
35. W. Wu, Baseline studies of the clay minerals society source clays: Colloid and surface phenomena. *Clay. Clay. Miner.* **49**, 446–452 (2001).
36. S. K. Kundu, M. Yoshida, M. Shibayama, Effect of salt content on the rheological properties of hydrogel based on oligomeric electrolyte. *J. Phys. Chem. B.* **114**, 1541–1547 (2010).
37. S. Humbert, O. Lame, R. Séguéla, G. Vigier, A re-examination of the elastic modulus dependence on crystallinity in semi-crystalline polymers. *Polymer* **52**, 4899–4909 (2011).
38. S. Srivastava, J. H. Shin, L. A. Archer, Structure and rheology of nanoparticle–polymer suspensions. *Soft Matter* **8**, 4097 (2012).
39. A. A. Teran, R. Yuan, S. Mullin, N. P. Balsara, Discontinuous changes in ionic conductivity of a block copolymer electrolyte through an order–disorder transition. *ACS Macro Lett.* **1**, 305–309 (2012).
40. R. Chiba, T. Ishii, F. Yoshimura, Temperature dependence of ionic conductivity in $(1-x)ZrO_2-(x-y)Sc_2O_3-yYb_2O_3$ electrolyte material. *Solid State Ion.* **91**, 249–256 (1996).
41. H.-J. Deiseroth, J. Maier, K. Weichert, V. Nickel, S.-T. Kong, C. Reiner, Li_7PS_6 and Li_6PS_5X (*X*: Cl, Br, I): Possible three-dimensional diffusion pathways for lithium ions and temperature dependence of the ionic conductivity by impedance measurements. *Z. Anorg. Allg. Chem.* **637**, 1287–1294 (2011).
42. N.-Q. Nguyen, A. J. C. Ladd, Sedimentation of hard-sphere suspensions at low Reynolds number. *J. Fluid Mech.* **525**, 73–104 (1999).
43. N.-Q. Nguyen, A. J. C. Ladd, Microstructure in a settling suspension of hard spheres. *Phys. Rev. E Stat.Nonlin. Soft Matter Phys.* **69**, 050401 (2004).
44. Y. Zhao, T. Zhou, D. Baster, M. el Kazzi, J. W. Choi, A. Coskun, Targeted functionalization of cyclic ether solvents for controlled reactivity in high-voltage lithium metal batteries. *ACS Energy Lett.* **8**, 3180–3187 (2023).
45. Z. Tong, B. Bazri, S.-F. Hu, R.-S. Liu, Interfacial chemistry in anode-free batteries: Challenges and strategies. *J. Mater. Chem. A* **9**, 7396–7406 (2021).
46. J. Qian, B. D. Adams, J. Zheng, W. Xu, W. A. Henderson, J. Wang, M. E. Bowden, S. Xu, J. Hu, J. G. Zhang, Anode-free rechargeable lithium metal batteries. *Adv. Funct. Mater.* **26**, 7094–7102 (2016).
47. Y. Tian, Y. An, C. Wei, H. Jiang, S. Xiong, J. Feng, Y. Qian, Recently advances and perspectives of anode-free rechargeable batteries. *Nano Energy* **78**, 105344 (2020).
48. T. Liu, S. Zhao, Q. Xiong, J. Yu, J. Wang, G. Huang, M. Ni, X. Zhang, Reversible discharge products in Li–Air batteries. *Adv. Mater.* **35**, 2208925 (2022).
49. Y. Qiao, K. Jiang, H. Deng, H. Zhou, A high-energy-density and long-life lithium-ion battery via reversible oxide–peroxide conversion. *Nat. Catal.* **2**, 1035–1044 (2019).
50. K. A. Wood, G. Teeter, XPS on li-battery-related compounds: Analysis of inorganic SEI phases and a methodology for charge correction. *ACS Appl. Energy Mater.* **1**, 4493–4504 (2018).
51. S.-K. Otto, Y. Moryson, T. Krauskopf, K. Peppler, J. Sann, J. Janek, A. Henss, In-depth characterization of lithium-metal surfaces with XPS and ToF-SIMS: Toward better understanding of the passivation layer. *Chem. Mater.* **33**, 859–867 (2021).
52. A. L. Bard, *Electrochemical Methods Fundamentals and Applications*, (John Wiley & Sons, 2001).
53. Q. Zhao, X. Liu, J. Zheng, X. Deng, A. Warren, Q. Zhang, L. A. Archer, Designing electrolytes with polymerlike glass-forming properties and fast ion transport at low temperatures. *Proc. Natl. Acad. Sci. U.S.A.* **117**, 26053–26060 (2020).
54. W. Li, H. Yao, K. Yan, G. Zheng, Z. Liang, Y.-M. Chiang, Y. Cui, The synergetic effect of lithium polysulfide and lithium nitrate to prevent lithium dendrite growth. *Nat. Commun.* **6**, 7436 (2015).

Acknowledgments

Funding: This work was supported by the Department of Energy Basic Energy Sciences Program through Award DE-SC0016082. The study also made use of the facilities and instrumentation supported by NSF through the Cornell University Materials Research Science and Engineering Center DMR-1719875. **Author contributions:** N.W.U. and L.A.A. contributed to the design of the research and experimental data analysis. N.W.U. prepared electrolyte materials and conducted electrochemical testing and materials characterization. R.S. conducted and analyzed XPS measurements. S.H. and Y.D. performed SEM characterization. P.O measured particle size and aided in TGA measurement. XRD was conducted by K.-i.K., and Raman spectroscopy was conducted by R.G.-M. M.G.K. aided in material preparation. L.A.A. and Y.L.J. supervised the work. All the authors discussed the results and commented on the manuscript. **Competing interests:** N.W.U. and L.A.A. are inventors on a patent application related to this work filed by Cornell University (NO. 63/618,742, filed 8 January 2024). The other authors declare that they have no competing interests. **Data and materials availability:** All data needed to evaluate the conclusions in the paper are present in the paper and/or the Supplementary Materials.

Submitted 3 February 2024
Accepted 4 June 2024
Published 5 July 2024
10.1126/sciadv.ado4719